ADVANCED ENERGY MATERIALS
www.advenergymat.de

Unveiling the Role of Ruthenium in Layered Sodium Cobaltite Toward High-Performance Electrode Enabled by Anionic and Cationic Redox

Natalia Voronina, Konstantin Köster, Jun Ho Yu, Hee Jae Kim, Min-Gi Jung, Hun-Gi Jung, Kug-Seung Lee, Payam Kaghazchi, and Seung-Taek Myung**

The effect of Ru substitution on the structure and electrochemical properties of P2-type $Na_{0.67}CoO_2$ is investigated. The first-discharge capacities of $Na_{0.67}CoO_2$ and $Na_{0.6}[Co_{0.78}Ru_{0.22}]O_2$ materials are 128 and 163 mAh g^{-1} (23.5 mA g^{-1}), respectively. Furthermore, the rate capability is improved due to the electro-conducting nature of Ru doping. Operando X-ray diffraction analysis reveals that the $Na_{0.67}CoO_2$ does not undergo a phase transition; however, multiple Na^+/vacancy ordered superstructures within the P2 phase appear during Na^+ extraction/insertion. In contrast, the $Na_{0.6}[Co_{0.78}Ru_{0.22}]O_2$ material undergoes a P2–OP4 phase transition during desodiation, with no formation of Na^+/vacancy ordering within the P2 phase. The increased discharge capacity of $Na_{0.6}[Co_{0.78}Ru_{0.22}]O_2$ is most likely associated with additional cationic Ru^{4+}/Ru^{5+} redox and increased anionic $O^{2-}/(O_2{}^{n-})$ redox participation. Combined experimental (galvanostatic cycling, X-ray absorption spectroscopy, differential electrochemical mass spectrometry) and theoretical (density functional theory calculations) studies confirm that Ru substitution provokes the oxygen-redox reaction and that partial O_2 release from the oxide lattice is the origin of the reaction. The findings provide new insight for improving the electrode performance of cathode materials via 4*d* Ru substitution and motivate the development of a new strategy for the design of high-capacity cathode materials for sodium-ion batteries.

1. Introduction

Layered Na_xCoO_2 attracted significant interest in the early 1980s because of their promising thermoelectric applications and diverse physical properties.[1,2] Moreover, for battery applications, investigation of their electrochemical properties was pioneered by Delmas et al.[3–5] These researchers summarized the crystal structure of Na_xCoO_2 depending on the Na content; namely, O3 (α), O'3 (α'), P'3 (β), and P2 (γ) phases.[5] The four main structural forms (α, α', β, and γ) differ in terms of the coordination of sodium atoms (octahedral O (α and α') or trigonal prismatic P (β and γ)) and the corresponding stacking sequence of the close-packed oxygen layers. O-type structures intrinsically provide a high sodium content, which is advantageous in achieving high energy density and high coulombic efficiency (CE) at the first cycle.[6] However, the voltage profile possesses complex behavior with several flat and sloping regions, which follow the sequence of O3–O'3–P'3–P3–P'3 phase transformations on charge, increasing the resulting *c*-lattice parameter.[5] P-type compounds undergo mitigated phase transformations during de-/sodiation, although Na^+/vacancy orderings are observed with Na contents within the P2 phase, such as x in Na_xCoO_2 (x = 0.5, 0.57, 0.66, 0.72, and 0.79), according to a report by Delmas et al.[7] These two features are related to capacity fade on subsequent cycles; therefore, the substitution of Co with

N. Voronina, J. H. Yu, H. J. Kim, S.-T. Myung
Hybrid Materials Research Center
Department of Nano Technology and Advanced Materials Engineering
Sejong Battery Institute
Sejong University
Seoul 05006, South Korea
E-mail: smyung@sejong.ac.kr

K. Köster, P. Kaghazchi
Forschungszentrum Jülich GmbH Institute of Energy and Climate Research Materials Synthesis and Processing
IEK-1 52425 Jülich, Germany
E-mail: p.kaghazchi@fz-juelich.de

The ORCID identification number(s) for the author(s) of this article can be found under https://doi.org/10.1002/aenm.202302017

M.-G. Jung, H.-G. Jung
Center for Energy Storage Research
Korea Institute of Science and Technology
Seoul 02792, South Korea

K.-S. Lee
Pohang Accelerator Laboratory
80 Jigokro-127-beongil, Nam-gu, Pohang, Gyeongbuk 37673, South Korea

P. Kaghazchi
MESA+ Institute for Nanotechnology University of Twente Enschede
Twente Enschede 7500 AE, The Netherlands

DOI: 10.1002/aenm.202302017

electroactive elements (Ni[8] and Mn[9–11]) or inactive elements (Ti[12–14] and Ca[15,16]) has been exploited to increase the capacity, mitigate the phase transition, and prevent degradation of P2-Na_xCoO_2 during the de-/sodiation process.

For example, Ceder et al.[8] investigated Ni-doped P2-$Na_x[Co_{0.78}Ni_{0.22}]O_2$, which provides a first discharge capacity of ≈134 mAh g^{-1} with 54% retention over 200 cycles at 0.1 C. Apart from the Na^+ extraction associated with a single-phase reaction on desodiation, the corresponding Na^+ insertion progressed via two stages: a two-phase reaction for the Na-deficient state ($Na_x[Co_{0.78}Ni_{0.22}]O_2$, $x = 0.2$–0.4) followed by a single-phase reaction in the range of $x = 0.4$–0.75 in $Na_x[Co_{0.78}Ni_{0.22}]O_2$. However, the raising of the operation voltages associated with the Ni^{3+}/Ni^{4+} redox couple was not observed due to the domination of the repulsive Na^+–Na^+ interaction in the sodiated state. Mn substitution is also noteworthy because of its widespread use; for instance, a Mn-substituted P2-$Na_{2/3}[Co_{2/3}Mn_{1/3}]O_2$ cathode presented a smooth voltage profile in the range of 1.5–4 V.[9] Nevertheless, increasing the Mn content was not promising in terms of capacity retention because of the structural instability resulting from Jahn–Teller distortions of Mn^{3+} ions in the structure and the low operation voltage stemming from the Mn^{4+}/Mn^{3+} redox reaction.[11]

The introduction of electro-inactive moieties has undoubtedly resulted in improved physical properties of active materials and electrode performance. Ti is a widely accepted substituent despite the empty 3*d* orbital of Ti^{4+}, whereas the inactivity stabilizes the oxide structure,[12] as the corresponding Gibbs free energy of formation at 298 K for TiO_2 is as low as −888 kJ mol^{-1}.[13] The stability assisted by Ti substitution in P2-Na_xCoO_2 boosts its long-term cyclability even in the presence of Na^+/vacancy ordering mitigation.[13,14] More efforts have been made to stabilize the structure of P2-Na_xCoO_2 by substituting the prismatic Na sites with Ca^{2+} (1.00 Å), which has a similar ionic radius to Na^+ (1.02 Å).[15,16] The immobile Ca^{2+} was demonstrated to partially suppress the formation of numerous Na^+/vacancy ordered phases, resulting in stable electrochemical performance during cycling.[16] However, it is possible that facile migration of Na^+ may be impeded by the presence of Ca^{2+} in the prismatic Na sites. In addition, the divalent ion can result in a decrease in the first charge capacity as it induces an increase in the average oxidation states of transition metals toward 4+.

From the above viewpoint, engineering of the transition-metal layer appears to be critical to stabilizing the crystal structure during Na^+ de-/intercalation to avoid hindering the facile Na^+ migration. In addition, the activity of the *d*-orbital electrons is also an important issue to support capacity improvement. The element of *4d* Ru, along with *5d* Ir and *3d* Mn, is recognized as one of the elements in promoting oxygen redox reaction. Regardless of the structure type of layered sodium cathodes, such as deficient P2-type[17] or stoichiometry O3-,[18,19] or alkali-rich O3-[20,21] phases, the presence of Ru is known to facilitate oxygen redox reaction once the oxidation state of Ru reaches 5+. This is attributed to the stronger covalent bond between 4*d* Ru—O compared to 3*d* TM—O bonds, typically leading to a stable oxygen redox reaction. Another significant characteristic of the *4d* Ru element is its ability to lower the operating voltage for oxygen redox (≈4.0–4.2 V), compared to Mn-based compounds (≈4.2–4.4 V).[22] This voltage reduction helps prevent electrolyte decomposition at high voltages and improves electrochemical performance assisted by both TM and O redox. One possible mechanism for oxygen redox involves the hybridization of Ru *d*-orbitals with O *p*-orbitals. This orbital overlap endorses facile electron transfer between the Ru and O atoms, realizing the participation of lattice oxygen in electrochemical redox process. Overall, these differences highlight the efficacy of Ru in promoting oxygen redox reaction and improving the electrode performance. To address these concerns, we have attempted to stabilize the crystal structure during Na^+ de-/sodiation and increase the capacity of $Na_{0.67}CoO_2$ using tetravalent 4*d* Ru, namely, P2-type $Na_{0.6}[Co_{0.78}Ru_{0.22}]O_2$ (NCRO). The tetravalent Ru not only is electrochemically active and contributes to additional capacity but also improves the electrical conductivity of the active material.[23] As designated, we observed an increase of the capacity from 128 mAh (g-oxide)$^{-1}$ for NCO to 163 mAh (g-oxide)$^{-1}$ at 23.5 mA g^{-1} for the Ru-substituted $Na_{0.6}[Co_{0.78}Ru_{0.22}]O_2$, which was enabled by the contribution of additional redox pairs by Ru^{5+}/Ru^{4+} and anionic $O^{2-}/(O_2^{n-})$ in addition to the Co^{4+}/Co^{3+}, as evidenced by X-ray absorption near-edge structure (XANES) spectroscopy. According to the observation by operando X-ray diffraction (*o*-XRD), it is also emphasized for the NCRO electrode that the Ru substitution successfully suppressed the emergence of Na^+/vacancy ordering, although the associated phase transition from P2 to OP4 was evident on desodiation and vice versa on sodiation. This absence of ordering would result from the presence of covalency by the Ru^{5+}—O bond in the oxide matrix during de-/sodiation, which plays an important role in stabilizing the crystal structure. Therefore, the $Na_{0.6}[Co_{0.78}Ru_{0.22}]O_2$ was able to retain the capacity of 77% for 200 cycles. We herein report on the efficacy of Ru substitution to stabilize the crystal structure of P2-type Na_xCoO_2.

2. Results and Discussion

Figure 1a,b-1,b-2 presents crystal structure and XRD patterns of the as-synthesized P2-type $Na_{0.67}CoO_2$ (NCO) and $Na_{0.6}[Co_{0.78}Ru_{0.22}]O_2$ (NCRO) powders, refined using the hexagonal lattice with $P6_3/mmc$ space group (JCPDS card No. 87–0274). The resulting structures determined from the refinement are illustrated in Figure 1a. No superstructure peaks appeared in the range of 18°–30° (2θ) for either material, which implies a disordered Co/Ru arrangement in the TM layer. According to the structural refinements by the Rietveld method, the *a*- and *c*-lattice parameters and *V* increased after Ru substitution (Table S1, Supporting Information). These variations may be related to the oxidation states of the transition-metal elements; hence, we conducted XANES analysis for the as-synthesized NCO and NCRO products (Figure 1c). For the Ru K-edge spectra, the average oxidation state of Ru was close to Ru^{4+} (Figure 1c-1). The photon energy of the Co K-edge shifted toward lower energy for the NCRO, implying a slight decrease in the oxidation state of Co induced by the Ru substitution (Figure 1c-2). This tendency explains the increase in the lattice parameter by the Ru substitution. Namely, Ru^{4+} ($t_{2g}^4 e_g^0$, 0.62 Å) prefers to occupy the Co^{4+} site ($t_{2g}^5 e_g^0$, high spin, 0.53 Å) rather than the Co^{3+} site ($t_{2g}^6 e_g^0$, low spin, 0.545 Å) for charge balance, as the average oxidation state of Co was lowered. This result implies replacement of Co^{4+} by Ru^{4+} in the NCRO compound. In the NCO compound, Co

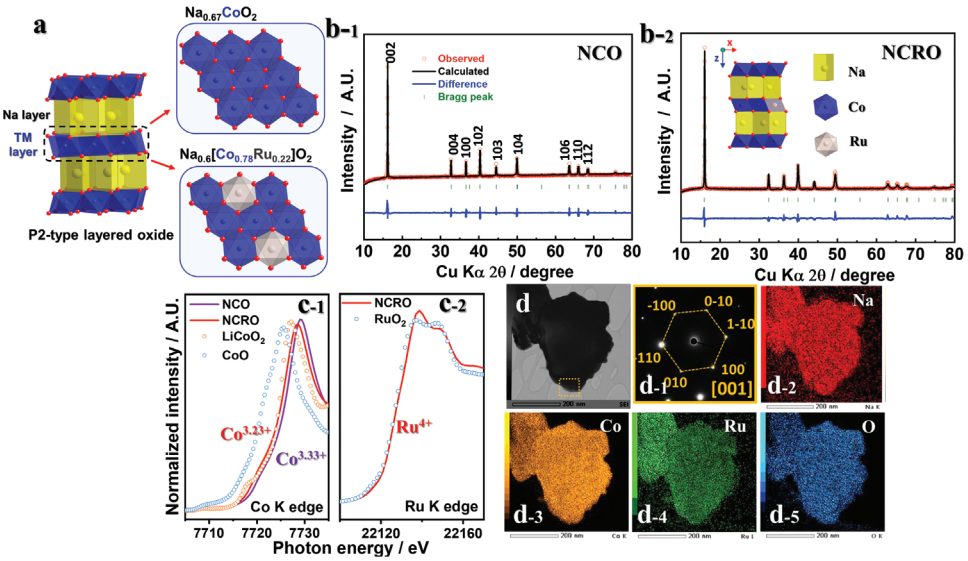

Figure 1. a) Schematic illustration of NCO and NCRO crystal structures, b) Rietveld refinement of powder XRD patterns for b-1) $Na_{0.67}CoO_2$ and b-2) $Na_{0.6}[Co_{0.78}Ru_{0.22}]O_2$ (inset: P2 crystal structure of NCRO). c) XANES spectra of c-1) Co K-edge, c-2) Ru K-edge NCO, and NCRO compounds. d) TEM of $Na_{0.6}[Co_{0.78}Ru_{0.22}]O_2$ with corresponding d-1) SAED pattern along [001] zone axis and EDS mapping d-2–d-5).

exists as Co^{3+} and Co^{4+} in a 2:1 ratio ($Co^{3.33+}$). For the NCRO compound, Ru is stabilized as Ru^{4+}; hence, Co emerges with Co^{3+} and Co^{4+} in a ratio of 3.33:1 ($Co^{3.23+}$). Therefore, the corresponding chemical formula can be rewritten as $Na_{0.67}[Co_{0.33}{}^{4+}Co_{0.67}{}^{3+}]O_2$ and $Na_{0.6}[Ru_{0.22}{}^{4+}Co_{0.18}{}^{4+}Co_{0.6}{}^{3+}]O_2$ for NCO and NCRO, respectively.

The morphologies of the as-synthesized NCO and NCRO particles were observed using FE-SEM and HRTEM (Figure 1d; Figures S1 and S2, Supporting Information). Both powders exhibited similar morphologies (Figure S1, Supporting Information). In addition, the TEM-EDX mapping data of NCRO clearly shows the presence of Na, Co, Ru, and O elements, which are uniformly distributed throughout the sample (Figure 1d; Figure S2, Supporting Information). The selected-area electron diffraction (SAED) pattern along the [001] zone axis indicates that the structure of NCRO was highly crystalline and stabilized in the hexagonal symmetry.

NCO and NCRO composite electrodes were evaluated in the voltage range of 1.5–4.3 V at a constant current of 23.5 mA g^{-1} (0.1 C). The NCO and NCRO electrodes delivered first-charge (oxidation) capacities of 107 and 128 mAh g^{-1}, which is consistent with ≈0.42 and 0.55 mol of Na^+ extraction, respectively (Figure 2a,b). The NCO material exhibited a complicated stair-wise voltage profile with numerous plateaus (2.73, 2.98, 3.28, 3.66, and 3.98 V) during the first charge; this behavior has been previously reported in literature.[7] The process is attributed to the different Na^+/vacancy ordering rearrangements resulting from the strong coulombic interaction induced by vacancies and Na^+ ordering in the sodium layers. In contrast, it is notable that the NCRO electrode demonstrates a smooth sloppy charge profile up to 4.0 V, followed by a flat plateau at 4.15 V (Figure 2b). The emergence of a sloppy charge profile instead of stair-wise progress up to 4.0 V results from the suppression of Na^+/vacancy ordering transitions during Na^+ extraction from the host structure. In addition, the flat plateau that emerged at 4.15 V implies the occurrence of oxidation of lattice oxygen (O^{2-} to $(O_2)^{n-}$, n < 2). Indeed, the dQ/dV curves showed numerous peaks for NCO and only one peak for NCRO on charge (Figure 2c,d), which agree with the CV data for NCO and NCRO (Figure S3, Supporting Information). On the first discharge, the NCO material displayed even more plateaus than on charge (3.94, 3.63, 3.24, 2.93, 2.65, 2.52, 2.4, and 2.32 V), which are related to the Na^+/vacancy ordering (Figure 2c; Figure S3, Supporting Information). The NCRO electrode demonstrates smooth decay of the operation voltage (Figure 2d). Figure 2e,f presents continuous charge–discharge curves tested at 0.1 C for 200 cycles, with significant improvement in the capacity retention as cycling progressed for the Ru-substituted one. It is believed that this improvement is related to the structural stability resulting from the electro-active Ru^{4+} substitution (Figure 2g). The rate capability also confirms the efficacy of Ru substitution over the tested current range from 0.1 C (23.5 mA g^{-1}) to 20 C (4.7 A g^{-1}) (Figure 2h–j). The better electronic conductivity of NCRO is responsible for the improved rate performance, namely, 5×10^{-5} S cm^{-1} for NCO and 3×10^{-4} S cm^{-1} for NCRO measured by the four-point DC method. Furthermore, to analyze the gradual capacity fading in NCO and NCRO electrodes, we measured ac-impedance in a half-cell configuration (Figure S4, Supporting Information). The impedance measurements were conducted for the fresh state, after the first discharge, and after the 200th discharge for NCO and NCRO cells. The charge-transfer resistance of NCRO was estimated to be lower than that of NCO at the fresh state. And, the charge-transfer resistance of NCRO was also lower than that of NCO after the 1st and 200th discharge, confirming that the Ru substitution is effective in improvement on electrochemical performance. Summarizing the above electrochemical properties, it is evident that Ru^{4+} plays a significant role in stabilizing the structure by suppressing Na^+/vacancy ordering during cycling, with an additional contribution to conductivity for improved rate performance.

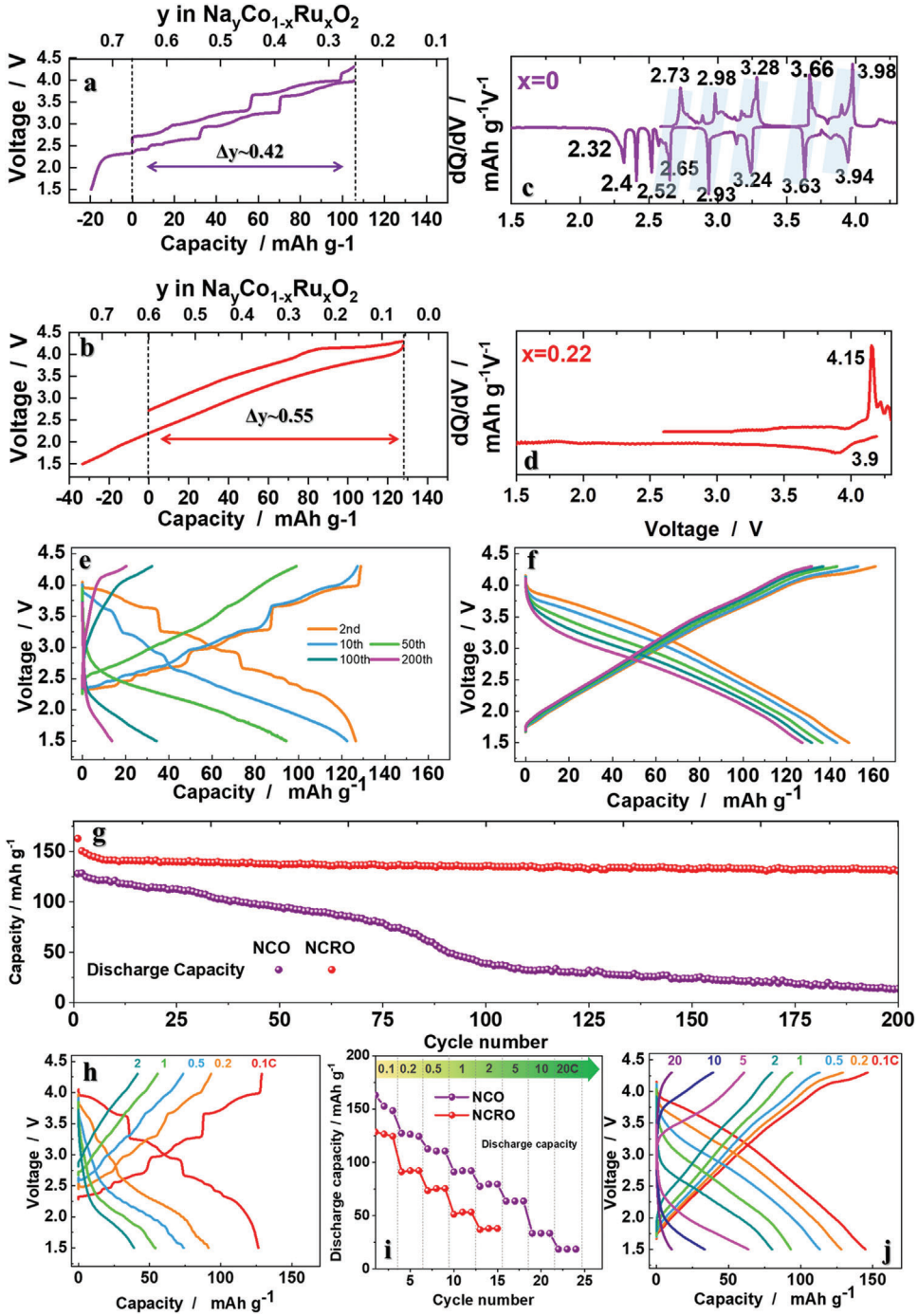

Figure 2. The first charge–discharge curves of a) NCO and b) NCRO measured at a current of 23.5 mA g−1 (0.1 C) in the voltage range of 1.5–4.3 V at 25 °C. Differential capacity plot of c) NCO and d) NCRO. Charge/discharge curves of e) NCO and f) NCRO at different cycles. g) Cycle life for both electrodes. Charge/discharge curves at different current densities from 0.1 (23.5 mA g^{-1}) to 20 C (4.7 A g^{-1}) for h) NCO and j) NCRO. i) Rate performance for both electrodes at different current densities.

Assuming the 1 mole Na^+ transfer (insertion of Na^+ into the structure: $Na_{1.0}CoO_2$ and $Na_{1.0}$ $[Co_{0.78}Ru_{0.22}]O_2$ formulae) in the formula unit, the calculated theoretical capacity to be 252 mAh g^{-1} for NCO and 235 mAh g^{-1} for NCRO. For charge (assuming extraction of 0.6Na^+) of $Na_{0.6}[Co_{0.78}Ru_{0.22}]O_2$, the calculated theoretical capacity is 141 mAh g^{-1} to be $Na_0[Co_{0.78}Ru_{0.22}]O_2$, for which the observed capacity by Na^+ extraction from the host structure was 128 mAh g^{-1} that results in $Na_{0.06}[Co_{0.78}Ru_{0.22}]O_2$ (extraction of Na^+ of ≈0.54 mol). So, the obtained capacity did not exceed the theoretical limit for the charging process. For discharge (insertion of Na^+) in the composition of $Na_{0.06}[Co_{0.78}Ru_{0.22}]O_2$, the delivered capacity was

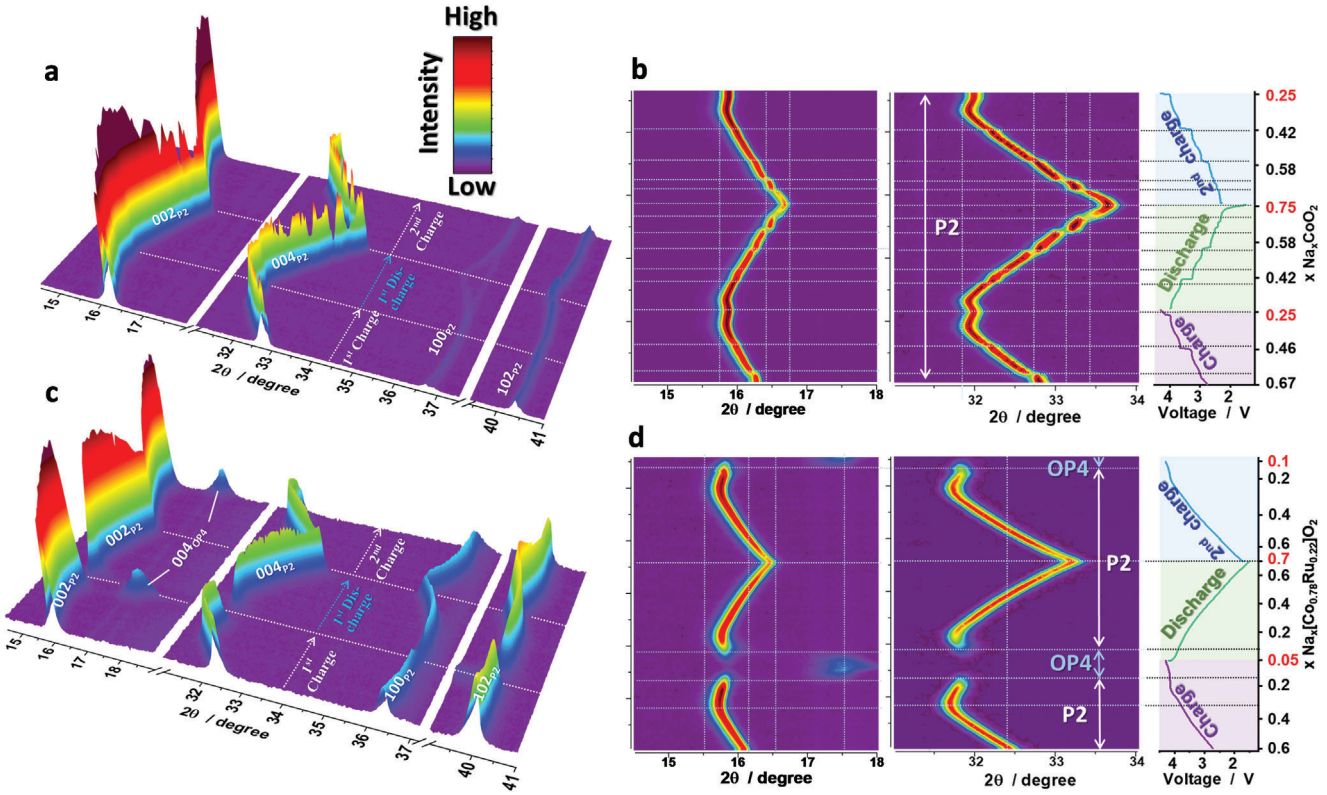

Figure 3. *3D* operando XRD data collected during the first 1.5 cycles for a) NCO and c) NCRO. *2D* operando XRD data and 1st charge/1st discharge/2nd charge curves for b) NCO and d) NCRO.

≈163 mAh g^{-1}. So, the inserted Na^+ into the host structure was ≈0.69 mol, giving $Na_{0.75}[Co_{0.78}Ru_{0.22}]O_2$. The value is also within the theoretical limit of 235 mAh g^{-1}. The small first charge capacity observed in NCRO cathode material with relatively low coulombic efficiency (≈78.5%) resulted from the sodium deficiency in the structure (0.6Na per formula unit). This phenomenon is typically observed for sodium-deficient P2-/P3-type cathodes. However, we believe that this issue can be resolved to enable full-cell application. Possible approaches to address this challenge are presodiation of the cathodes using sacrificial sodium additives. These additives supply additional sodium ions to the anode during the initial charging process through the oxidative decomposition of the sacrificial agent at high voltage. It becomes feasible to achieve high coulombic efficiencies close to 100% during the first cycle. Various sacrificial agents, including compounds such as NaN_3,[24] Na_3P,[25] Na_2CO_3,[26] and diethylenetriamine penta-acetic acid salt (DTPA-5Na),[27] have been investigated to provide supplementary sodium ions during the first charge. Therefore, the low first charge capacity of P2-$Na_{0.6}[Co_{0.78}Ru_{0.22}]O_2$ cathode can be compensated by sacrificial agents.

Operando XRD (*o*-XRD) measurements were conducted to understand the phase evolution for the NCO (Na_xCoO_2, $x = 0.67$) and NCRO ($Na_x[Co_{0.78}Ru_{0.22}]O_2$, $x = 0.6$) electrodes upon Na^+ extraction and insertion (**Figure 3**). The chemical compositions of NCO and NCRO electrodes at the fresh, fully charged (4.3 V), and fully discharged (1.5 V) states were analyzed using inductively coupled plasma-atomic emission spectroscopy (ICP-AES) (Table S2, Supporting Information), and the results were in good agreements with our capacity-derived results. For the Ru-free Na_xCoO_2 ($x = 0.67$), desodiation resulted in a gradual shift of the $(002)_{P2}$ and $(004)_{P2}$ Bragg peak positions at 16.2° and 32.5° (2θ) toward lower angles, whereas the $(100)_{P2}$ and $(102)_{P2}$ peaks at 36.7° and 40.4° (2θ) shifted toward higher angles in the range of $0.25 \leq x \leq 0.67$ for Na_xCoO_2 within the P2 phase (Figure 3a,b; Figure S5a, Supporting Information). Specifically, the desodiation results in the formation of several single-phase domains $0.6 \leq x \leq 0.67$, $0.46 \leq x \leq 0.6$, and $0.25 \leq x \leq 0.46$ in Na_xCoO_2, which correspond to Na^+/vacancies orderings. Upon further desodiation, $x \leq 0.25$ in Na_xCoO_2 was also progressed via a single-phase reaction, maintaining the P2 phase without any sign of O2 or OP4 phase (the intergrowth of O2–P2) formation. The single-phase reaction at the highly desodiated states emerged with shifts of the $(002)_{P2}$ and $(004)_{P2}$ peaks to lower angles, whereas the $(100)_{P2}$ and $(102)_{P2}$ peaks did not show significant shifts to the end of charge to 4.3 V. On discharge, several single-phase domains were observed at $0.25 \leq x \leq 0.4$, $0.4 \leq x \leq 0.54$, and $0.54 \leq x \leq 0.6$ in Na_xCoO_2, which are reversible in comparison to the charge process. At lower voltages of $0.6 \leq x \leq 0.68$, $0.68 \leq x \leq 0.75$ in Na_xCoO_2, two additional sequences of the ordered Na^+/vacancies arrangements were clearly detected within the P2 phase. Hence, the de-/sodiation of NCO material is progressed in the P2 framework with the formation of several Na^+/vacancy ordering arrangements (Figure 3b; Figure S2a, Supporting Information). Moreover, the phase-evolution behavior of NCO during the second charge is

identical to that of the first discharge, which progressed via the same Na^+/vacancies orderings.

For the $Na_x[Co_{0.78}Ru_{0.22}]O_2$ ($x = 0.6$), the observed phase transitions differ greatly from those observed for NCO (Figure 3c,d). For $0.3 \leq x \leq 0.6$ in $Na_x[Co_{0.78}Ru_{0.22}]O_2$, the Bragg peak positions for the P2 phase at 16.1° and 32.5° (2θ) moved to higher angles; however, the peaks at 36.4° and 40.4° (2θ) shifted to lower angles, similar to those of the NCO electrode. Further desodiation in the range of $0.1 \leq x \leq 0.3$ in $Na_x[Co_{0.78}Ru_{0.22}]O$ caused the $(002)_{P2}$ and $(004)_{P2}$ peaks to shift toward higher angles; however, there was less movement of the $(100)_{P2}$ and $(102)_{P2}$ peaks. Progressive deintercalation of Na^+ from the NCRO structure was observed along with the smoothened voltage profile, which indicates that the Ru substitution negated the occurrence of Na^+/vacancy ordering (Figure 3c). For $x = 0.15$ in $Na_xCo_{0.78}Ru_{0.22}O_2$, the emergence of the new OP4 phase at 17.4° (2θ) is inevitable, and the phase was maintained until the end of charge ($x = 0.05$ in $Na_xCo_{0.78}Ru_{0.22}O_2$). During sodiation, the formed OP4 phase was visible until $x = 0.15$ in $Na_xCo_{0.78}Ru_{0.22}O_2$, after which the phase was transformed into the P2 phase that was dominant until the end of discharge. Note that in comparison to the NCO material, the solid-solution process within the P2 phase progressed more smoothly without visible formation of Na^+/vacancy orderings (Figure 3c,d; Figure S5, Supporting Information).

From the *o*-XRD patterns, the lattice parameters were calculated using a least square method (**Figure 4**). For the NCO electrode (Figure 4a), desodiation accompanied a continuous decrease in the *a*-axis parameter, presumably due to the oxidation of Co^{3+} toward Co^{4+}, and an increase in the *c*-axis parameter, which is induced by the increased repulsive ionic-character interactions in the interlayer. The opposite tendency was observed during desodiation, namely an increase in the *a*-axis parameter but decrease in the *c*-axis parameter. The variation was ≈1.8% for the *a*-axis and 4.8% for the *c*-axis. The reversible behavior was also perceived during the second charge. For the Ru-substituted NCRO electrode (Figure 4b), the tendency, a decrease in the *a*-axis parameter but increase in the *c*-axis parameter, was similar to that of the NCO electrode. However, contraction of the *c*-axis was evident from $x \leq 0.3$ in $Na_xCo_{0.78}Ru_{0.22}O_2$, for which the structural transformation from the P2 to OP4 phase is responsible for the shrinkage of the interlayer distance as a result of the formation of the octahedron environment in the interlayer. Sodiation resulted in an increase of the *a*-axis parameter by ≈1.6% until the end of discharge. In parallel, the *c*-axis was expanded in the range of $0.05 \leq x \leq 0.3$ in $Na_xCo_{0.78}Ru_{0.22}O_2$, after which a gradual decrease in the *c*-axis parameter was observed until the end of discharge. Its variation was ≈4.1% for the P2 phase, which is slightly lower than the variation observed in the NCO electrode (4.8%). In summary, the *o*-XRD data clearly indicate that NCO and NCRO compounds undergo different structural transformations with several unique findings. For the NCO electrode, the P2 phase was maintained along with the emergence of several Na^+/vacancy orderings. In contrast, the Ru-substituted NCRO effectively prevents the Na^+/vacancy orderings within the P2 phase; however, it induces the phase transition from P2 to OP4 in the highly desodiated state. In addition, both the *a*- and *c*-axis parameters varied less within the P2 phase framework with the Ru substitution. Therefore, in the NCRO material, a reversible P2→OP4→P2 phase transition was observed without Na^+/vacancy orderings during de-/sodiation. (Figure 3c).

The electrochemical performance of NCO and NCRO cathode materials is affected by both the Na^+/vacancy ordering and P2-OP4-P2 phase transition. The doping of Ru can successfully suppress the Na^+/vacancy ordering in NCRO, although the P2-OP4-P2 phase transition still occurs due to the activation of oxygen redox at high voltage. This transition is accompanied by a noticeable variation in the *c*-axis parameter. However, the transition has minimal impact on the cycling performance due to good reversibility of the oxygen redox reaction, facilitated by the strong hybridization between 4*d* Ru and O. Interestingly, numerous studies have demonstrated excellent long-term cycling stability of cathode materials based on Mn and Ru, exhibiting P2-OP4-P2,[28,29] P2-Z-P2,[30] and even P2-Z-P2/P'2[17] phase transitions. Due to the large variation in the *c*-axis, the upper voltage cutoff was reduced to 4 V, for which a topotactic solid-solution reaction was progressed within the P2 structural framework (Figure S6, Supporting Information). Although the capacity was decreased to ≈132 mAh g^{-1} by lowering the charge cutoff voltage, the resulting capacity retention was ≈98% for 50 cycles. This indicates that there is no doubt that the additional capacity by the oxygen redox is beneficial to increase the capacity. Meanwhile, further elaboration is needed to progress the reaction within the stable P2 framework via structural stabilization of the *c*-axis by additional doping or surface modification in the presence of oxygen redox reaction for high voltage application.

Ex situ XANES analysis of the Co, Ru, and O K-edges was performed to probe the origin of the charge-compensation mechanism of both the NCO and NCRO electrodes (**Figure 5**). In comparison to the fresh NCO with desodiated electrodes, it is evident that the desodiation resulted in a shift of the resulting XANES spectra, namely, a shift of the pre-edge (≈7709 eV, 1*s*→3*d* transition) and white beam (main) (≈7729 eV, 1*s*→4*p* transition) spectra to higher-photon-energy position, which results from the oxidation of Co^{3+} toward Co^{4+}. One additional feature at ≈7720 eV responsible for the so-called "shakedown" process disappeared while charging to 4.3 V, which can be derived from the increased ionicity resulting in a decreased level of overlap between the O 2*p* orbitals and hybridized Co 3*d*–4*p* orbitals. Subsequent discharge of NCO led to a reduction of Co to the original state at ≈2.0 V and further toward Co^{3+} at the end of discharge to 1.5 V, indicating that Co is electrochemically active. Figure 5b presents the Co K-edge spectra for the NCRO material, showing a similar tendency for the pre-edge and white beam line spectra as for the NCO electrodes. The shoulder peak disappeared, confirming the oxidation of Co toward Co^{4+} on charge and vice versa on discharge. The Ru K-edge spectra present evident shifts toward higher photon energy, mostly in the voltage range of 2.5–3.5 V, and there was no change after charging to 4.3 V, corresponding to the high-voltage plateau (Figure 5c). This finding suggests that Ru^{4+} was oxidized toward Ru^{5+} mostly in the voltage range of 2.5–3.5 V that belongs to the sloping region. On discharge, the reaction was reversible, and the spectra moved toward the negative direction and eventually overlapped with the spectrum of the fresh NCRO electrode. To further prove the redox activity of Ru in NCRO, ex situ Ru 3*p* XPS was conducted at fresh, fully charged (4.3 V) and fully discharged (1.5 V) states (Figure S7, Supporting Information). The Ru $3p_{3/2}$ and Ru $3p_{1/2}$ core peaks are presented at 465 and

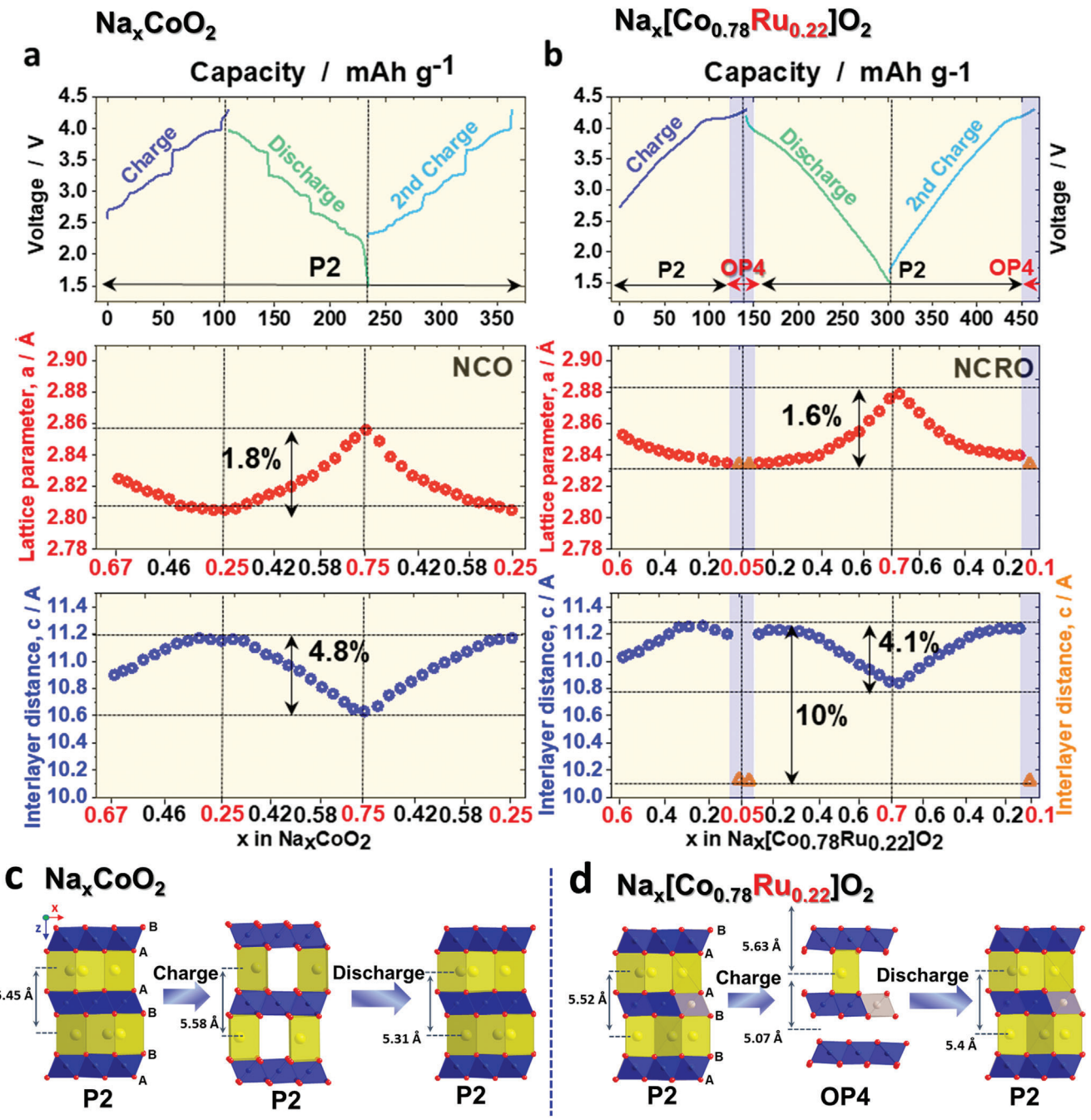

Figure 4. Calculated from the operando XRD results *a*- and *c*-axis parameters for a) NCO and b) NCRO; Schematic illustration of structural evolution of c) NCO and d) NCRO during the 1st cycle.

487 eV, respectively, corresponding to the Ru^{4+}—O binding energy in the NCRO electrodes. Upon charging, a noticeable shift was observed in the Ru 3*p* spectra. This finding is consistent with the XANES (Figure 5c) results that Ru is oxidized from 4+ toward 5+ during charge, in agreement with the result of Zhou et al.[19] Moreover, the binding energy of the Ru $3p_{1/2}$ core was recovered to the original position after discharging to 1.5 V, indicating the reversible Ru oxidation/reduction. In the O K-edge spectra, the pre-edge is characterized by two absorption peaks at ≈528.8 and ≈531.1 eV, which correspond to the transition of the O 1*s* state to the 3*d*/4*d* TM of the t_{2g} and e_g orbitals, respectively (Figure 5d,e). Upon charging to 4.3 V, a new shoulder at ≈530 eV emerged for the charged NCRO electrode, which belongs to the $(O_2)^{n-}$ (n <2) peak, associated with oxidation of O^{2-} to $(O_2)^{n-}$. This proves the oxidation of oxygen in the NCRO electrode. Note that the shoulder peak disappeared, and the resulting spectra were recovered to the original state. Therefore, it is suggested that the redox activities assisted by the Co^{4+}/Co^{3+}, Ru^{5+}/Ru^{4+}, and $O^{2-}/(O_2)^{n-}$ are

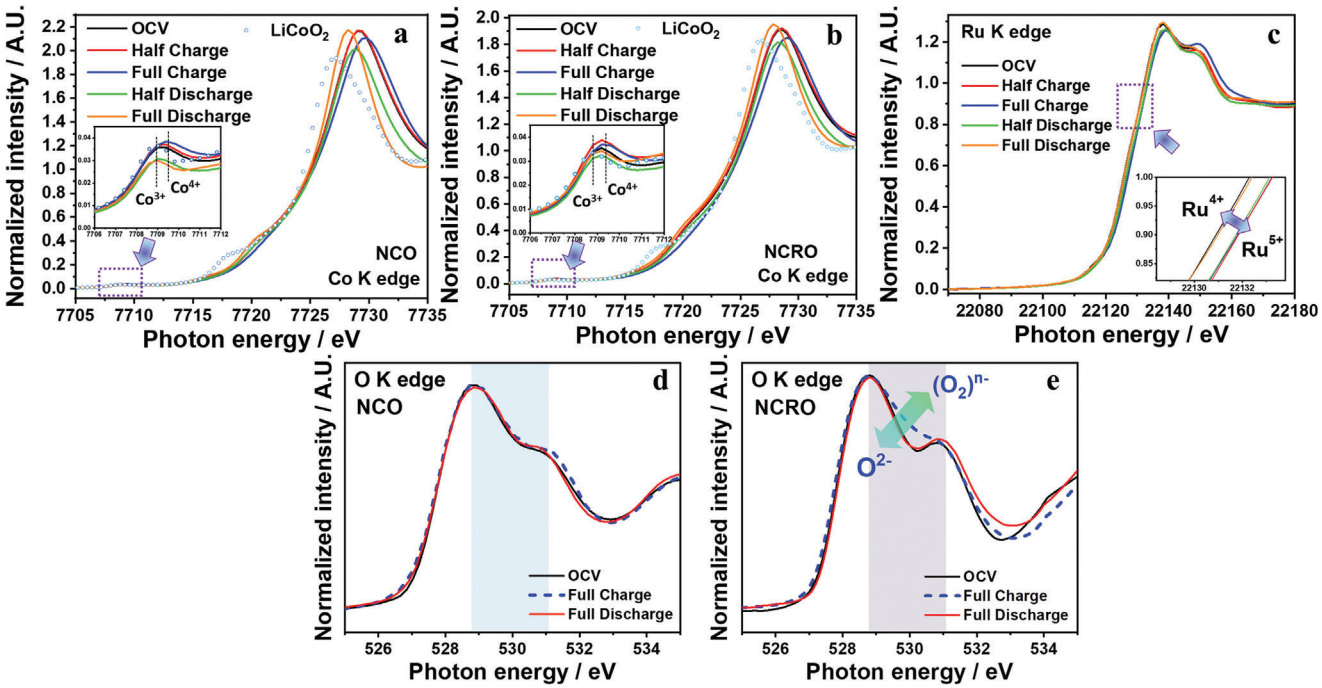

Figure 5. XANES spectra of Co K-edge for a) NCO, b) NCRO, and c) Ru K-edge for NCRO, O K-edge for d) NCO and e) NCRO.

responsible for additional Na^+ extraction and insertion, resulting in improved capacity of NCRO over NCO, which is solely activated by the Co^{4+}/Co^{3+} redox pair.

Galvanostatic intermittent titration technique (GITT) analysis was performed to compare the diffusion coefficients (D_{Na+}) of the NCO and NCRO electrodes (**Figure 6**a,b). Both electrodes exhibited reasonable diffusion coefficients in the operation range, with $\approx 10^{-10}$–10^{-11} cm^2 s^{-1}. For the NCO electrode, stepwise variation was observed at the border of Na^+/vacancy ordering regions during de-/sodiation (Figure 6a). However, the diffusion occurred smoothly to $x \approx 0.3$ in $Na_xCo_{0.78}Ru_{0.22}O_2$ (≈4.1 V) during desodiation, above which diffusion slowed down to $\approx 10^{-11}$ cm^2 s^{-1} as oxidation of oxygen progressed (Figure 6b). The delayed diffusion belongs to the region for the OP4 phase. Interestingly, the diffusivity was recovered to $\approx 10^{-10}$ cm^2 s^{-1} from $x \geq 0.2$ in $Na_xCo_{0.78}Ru_{0.22}O_2$ (≈3.8 V) in the P2-phase regime on sodiation. In comparison to other P2 layered materials, such as Ni- or Mn-based materials with oxygen redox,[17,20] the overpotential in NCRO at high voltage is much lower in magnitude, which is favored for faster anionic redox.

To overview the gas evolution from NCO and NCRO materials, operando differential electrochemical mass spectrometry (*o*-DEMS) measurements were conducted during the first cycle (Figure 6c,d). No significant O_2 gas evolution was detected from the NCO material. In contrast, the NCRO material underwent the release of O_2 gas at highly desodiated states, $x \leq 0.15$ in $Na_xCo_{0.78}Ru_{0.22}O_2$, where the OP4 phase was dominant. Correlating the O_2 release and emergence of the OP4 phase in this range, it is worth mentioning that the O_2 release provides an unpaired electron in O 2*p* orbitals, which can trigger the oxidation of oxygen. From this reaction, the extracted amount of Na^+ was ≈0.1 mol Na per formula unit in the range of $0.05 \leq x \leq 0.15$ in $Na_xCo_{0.78}Ru_{0.22}O_2$. Therefore, the increased extraction of Na^+ by the activity of oxidation of lattice oxygen induced the formation of the OP4 phase in the host structure. As oxidation of oxygen progresses rather sluggishly compared with that of TMs, the corresponding Na^+ diffusivity triggered by the oxygen activity appears to be slow. The above *o*-DEMS results allow qualitative estimation for O_2 evolution. This estimation aligns with our calculations that will be mentioned in **Figure 8**, indicating that strong oxidation of certain oxygen ions in the NCRO material could potentially lead to the formation of a peroxide or an oxygen dimer with subsequent O_2 gas release. Typically, the release of O_2 gas is detrimental to the stability of cathode materials. However, it has been widely observed in Li-rich materials[31] and sodium oxygen-redox cathode materials.[17] For instance, in the case of the Ru-based sodium cathode material P2-type $Na_{0.66}Li_{0.22}Ru_{0.78}O_2$, Zhou et al.[17] observed oxygen release at high voltage during the first cycle. However, on subsequent cycles, no irreversible oxygen loss was detected. Therefore, we also included the *o*-DEMS data for the NCRO material during the second cycle (Figure S8, Supporting Information), which clearly shows no evolution of O_2 gas. This indicates a reversible process associated with the oxygen redox in the NCRO material; hence, the formed vacancies in the lattice oxygen provide lone pair electron in O 2*p* orbital to trigger the oxygen redox.

We further elucidated the proposed redox mechanism and structural trends by applying density functional theory (DFT) calculations to the sodiated and desodiated phases for NCO and NCRO. Our DFT-PBE calculation confirms that the formation of the OP4 phase for the desodiated NCRO is energetically very close to that of the P2 phase (E(OP4)− E (P2) = 0.027 eV per formula unit). A comparable Ru-doping-induced change in the lattice parameters, as observed in the XRD patterns, was also

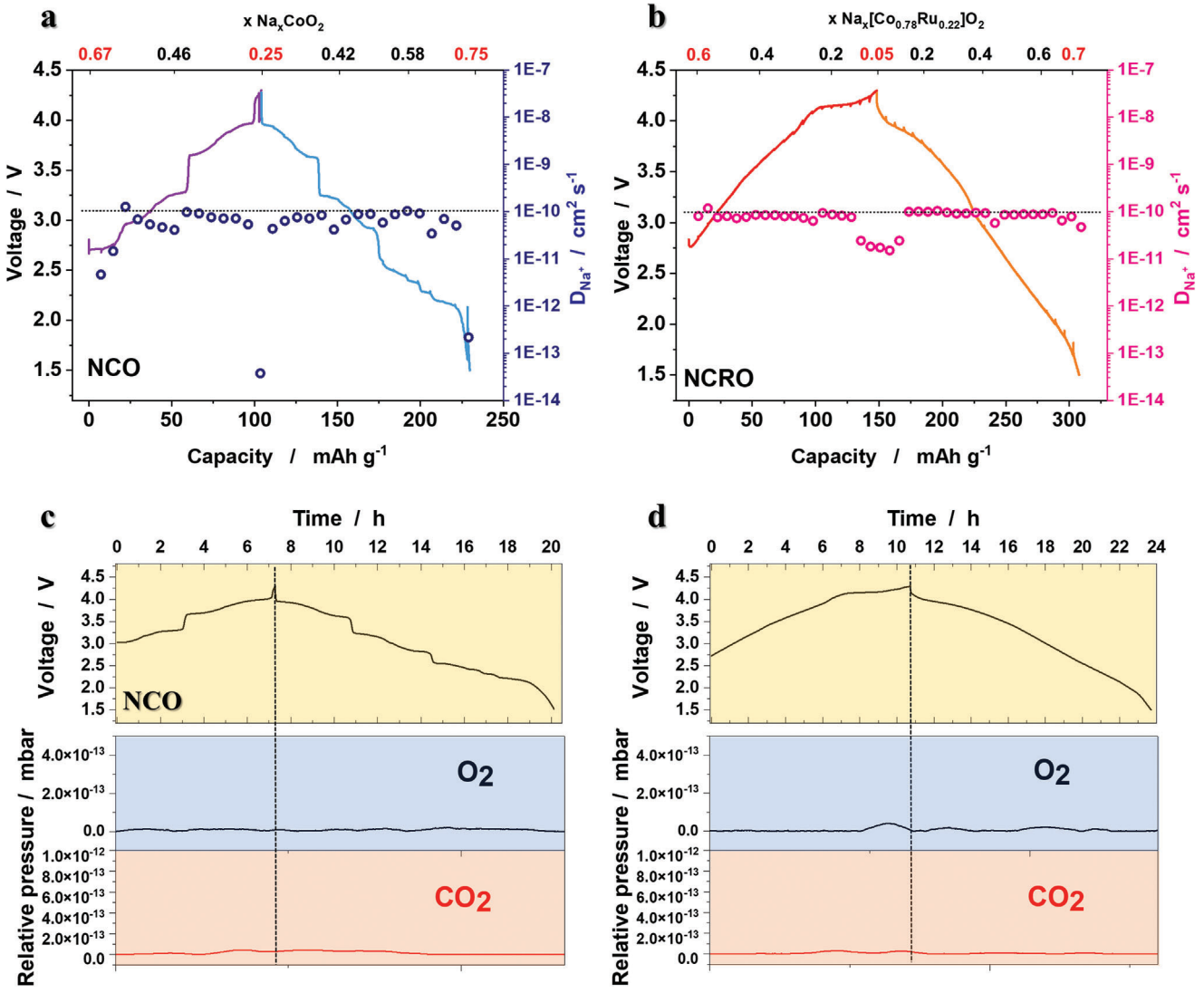

Figure 6. Charge/discharge voltage profiles and Na^+ diffusivity obtained from galvanostatic intermittent titration technique (GITT) for a) NCO and b) NCRO. *O*-DEMS results of gas evolution for O_2 and CO_2 tested using c) NCO and d) NCRO electrodes.

reproduced with our DFT-PBE calculation: although NCO shows a = 2.864 Å and c = 10.773 Å, NCRO was optimized to a = 2.909 Å and c = 10.919 Å. As already discussed in the experimental section, this increase can be explained by the larger ion radius of Ru^{4+} compared with that of Co^{4+}.

The computed total energies (per formula unit in Table S3, Supporting Information) with different total magnetic moments (number of unpaired electrons) with DFT-HSE06 do not differ greatly (ΔE<1 eV). This result could indicate a tendency to electron delocalization, which is in line with the fairly high electronic conductivities for the NCO and NCRO cathode materials observed using the four-point probe method. For all the materials, the solution with the lowest magnetic moment is the lowest in energy, indicating a tendency toward low-spin arrangements of the cobalt ions. Charge states were assigned to the ions by calculating their magnetic moments, which can also be visualized as spin density difference (SDD) plots, as shown for one metal layer of the investigated materials in **Figure 7** and Figure S9, Supporting Information. Interestingly, all parts with a significant number of unpaired electrons show the same spin direction. Especially for the sodiated materials (Figure 7a,c), it can be seen that there are no cobalt ions with magnetic moments remaining after doping with Ru. This state would correspond to Co^{3+} (low spin, $t_{2g}{}^6e_g{}^0$), whereas a cobalt ion with a magnetic moment of roughly "1" would correspond to Co^{4+} (low spin, $t_{2g}{}^5e_g{}^0$). The magnetic moments assigned to the cobalt ions are shown in Figure 8a. The Co^{4+}/Ru^{4+} replacement observed in the experiments matches the replacement of Co^{4+} by Ru^{4+} ions (Figure 7a,c). However, because of the slightly different composition used for the theoretical models, the results suggest an exchange of Co^{4+} by $Ru^{4.25+}$ ions. The assignment of a charge close to 4+ to the Ru ions can be again justified by a magnetic moment on the ions that is close to "2" (Figure 8), which corresponds to a low-spin $t_{2g}{}^4e_g$ configuration. Considering charge balance, this would yield the following formulas from

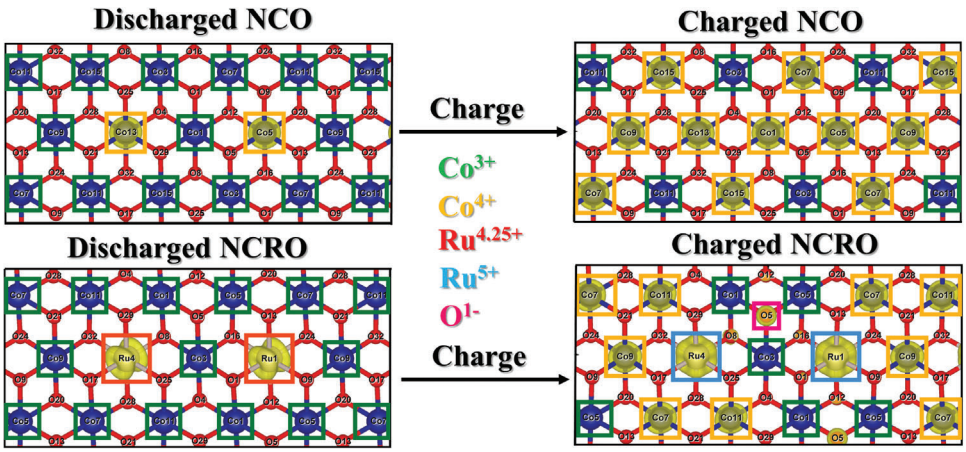

Figure 7. a) Spin density difference (SDD) plot of $N_{0.75}CO$, $N_{0.25}CO$, $N_{0.69}CRO$, and $N_{0.06}CRO$ at an iso-value of 0.05 unpaired electrons $Å^{-3}$. In general, the number of unpaired electrons increases on oxidation (charge) while the oxidation of cobalt is reduced on ruthenium doping. The oxidation of ruthenium can also be observed by the change in the shape of SDD located at the Ru ions.

the theoretical perspective for the discharged cathode materials: $Na_{0.75}[Co^{3+}{}_{0.75}Co^{4+}{}_{0.25}]O_2$ and $Na_{0.69}[Co^{3+}{}_{0.75}Ru^{4.25+}{}_{0.25}]O_2$. These proposed charges also match the calculated total magnetic moments of the supercells, as presented in Table S3 (Supporting Information).

On desodiation, an increase in the number of cobalt ions with a spin density close to 1 is observed, showing the activity of the Co^{3+}/Co^{4+} redox pair that was also observed in the experimental XANES studies. Therefore, the exchange of Co^{4+} by $Ru^{4.25+}$ also increases the activity of the Co^{3+}/Co^{4+} redox pair by forcing the cobalt ions to be 3+ in the discharged NCRO material. As the magnetic moments of oxygen undergo only minor changes (mostly less than 0.1) (Figure 8b), the redox activity in the NCO cathode can be exclusively assigned to the Co^{3+}/Co^{4+} redox pair with the calculations. This finding yields the following charge-balanced formula: $Na_{0.25}[Co^{3+}{}_{0.25}Co^{4+}{}_{0.75}]O_2$, which corresponds to the ratio of the number of cobalt ions with a magnetic moment of ≈0 (Co^{3+}) to that with a magnetic moment of ≈1 (Co^{4+}) in Figure 8a and also matches the calculated magnetic moment of 28.00 of the whole supercell (Table S3, Supporting Information).

The same redox pair is also active in NCRO according to the calculations; however, only half of the cobalt ions are oxidized from 3+ to 4 + on charge (Figure 8). Figure 8 also reveals a slight oxidation of Ru, as the number of unpaired electrons per ion increases from 1.79 to 2.18. This value is below the expected magnetic moment of 3 for Ru^{5+} ($t_{2g}{}^3e_g{}^0$). However, the change in the shape of the SDD in Figure 7c,d is quite severe. In addition, the magnetic moments on the oxygens reveal much more fluctuations in NCRO (Figure 8b) than in NCO, indicating a stronger oxidation of Ru to Ru^{5+}. Under this assumption, the fluctuations in the magnetic moments of oxygen would correspond to both the delocalization of oxidation of the ruthenium ions and the activation of oxygen redox in NCRO. These conclusions are also supported by the experimental findings that suggest the presence of Ru^{5+} as well as oxygen redox in the NCRO material. TMs are also highly oxidized toward Co^{4+} (0.53 Å) and Ru^{5+} (0.565 Å), which explains the Co^{4+}—O bond is stronger than the bond of Ru^{5+}—O due to the short distance with oxygen. This implies that the delocalization (forming lone pair electron) in Ru^{5+}—O is more favorable than that in Co^{4+}—O, as confirmed by the DFT calculation.

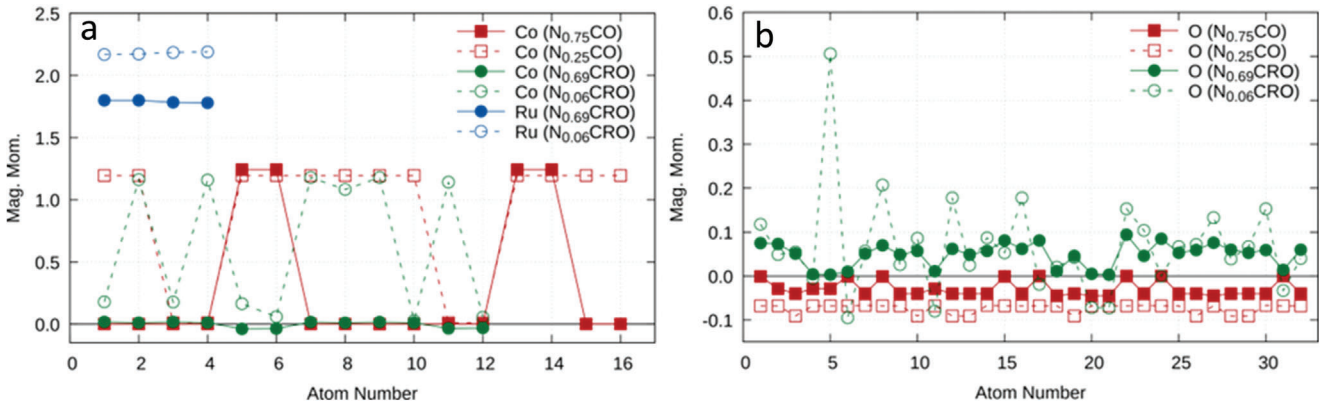

Figure 8. Magnetic moments of a) metals and b) oxygen for charged and discharged NCO and NCRO, atom numbers correspond to the numbers in Figure 7. It can be seen that the cobalt ions either have a magnetic moment of 0 (Co^{3+}) or 1 (Co^{4+}) and that the amount of Co^{4+} increases on charge. Oxidation of ruthenium is seen by the increase of ≈0.5 in the magnetic moment on desodiation. The magnetic moments of oxygens show more fluctuations in NCRO than in NCO indicating the activation of oxygen redox by the ruthenium doping.

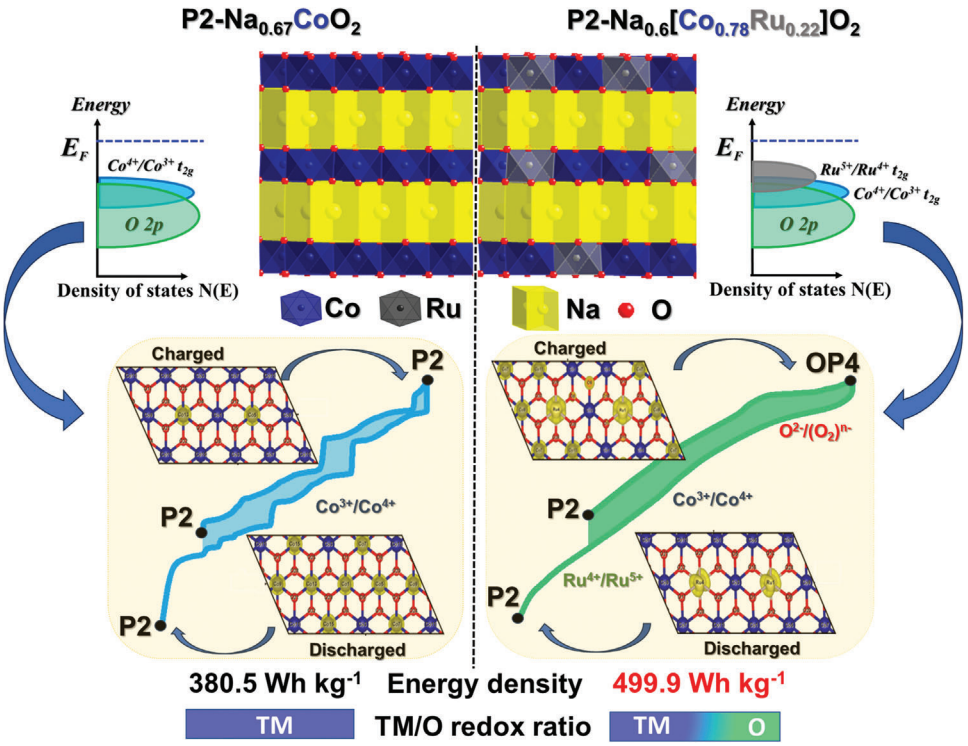

Figure 9. Schematic illustration of structure, phase transitions, and corresponding reaction mechanisms for NCO and NCRO.

Such that the observed evolution of oxygen in Figure 6d would be mainly ascribed to the oxygen bonded with Ru in the TM layer.

Next to the activation of (reversible) oxygen redox by ruthenium doping, the computational magnetic moments also reveal one very strongly oxidized oxygen ion (atom number 5 in Figure 8) with a magnetic moment of ≈0.5. This strong oxidation might indicate the beginning of the formation of an O^{1-} ion that could then continue to form a peroxide or an oxygen dimer eventually. Unfortunately, the formation of such a dimer for DFT geometry optimization is kinetically strongly hindered in NCRO and was therefore not observed in the calculations. However, the presence of such a strongly oxidized oxygen ion is in good agreement with the experimental *O*-DEMS measurements that revealed oxygen-gas release for NCRO, especially in comparison with NCO, where no oxygen gas was observed and for which the calculations show only minor magnetic moments (oxidation) on the oxygen ions. Taking all of this information into account, the following formula can be assigned to the charged NCRO material: $Na_{0.06}[Co^{3+}{}_{0.38}Co^{4+}{}_{0.38}Ru^{5+}{}_{0.25}][O_{0.06}{}^{1-}O_{1.94}{}^{2-}]$. Again, this composition ensures charge balance and would correspond to a magnetic moment of the simulated supercell of 19.0, which perfectly matches the value of 19.0 obtained in the calculations (Table S3, Supporting Information). Based on our DFT calculations, the redox processes can be summarized as follows: the activity of NCO appears to stem exclusively from the Co^{3+}/Co^{4+} redox, whereas that of NCRO originates from less Co^{3+}/Co^{4+} redox (compared to NCO) but additional Ru^{4+}/Ru^{5+} as well as $O^{2-}/(O_2)^{n-}$ redox. These findings are in good agreement with the experimental data and explain the observed superior performance of the NCRO cathode material compared with that of the NCO cathode material.

Our study explored the potential of Co substitution by Ru in layered P2-$Na_{0.67}CoO_2$ as an exciting and challenging strategy in the search for new materials. We concluded that Ru substitution allows for rational tailoring of electrochemical properties by mitigating Na^+/vacancy ordering and activating oxygen-redox phenomena. Despite the partial release of O_2 gas on the first charge, the NCRO material demonstrates higher capacity and energy density (NCO 380.5 Wh kg^{-1}, NCRO 499.9 Wh kg^{-1}) because of the involvement of all the Co, Ru, and O elements in the charge-compensation process and reasonable performance compared with that of the NCO material (**Figure 9**). In conventional sodium-ion battery cathode materials, the capacity is limited and usually delivered solely by TM redox reactions. However, recent studies have revealed that oxygen can also participate in electrochemical reactions, providing additional capacity and improving the overall performance of the battery. Therefore, in the current work, we verified the improved the capacity and rate capability of P2-$Na_{0.67}CoO_2$ cathode by Ru substitution (Table S4, Supporting Information). This paper aims to develop sodium-ion batteries with higher energy density by utilizing both cationic and anionic redox reactions, making them more competitive with other energy storage technologies. Our findings suggest a strategy for unlocking the electrochemical activity in the P2-Na_xCoO_2 framework via 4*d* element substitution, which can support the development of high-energy-density cathode materials.

3. Conclusion

In this study, the substitution of Ru in layered Na_xCoO_2 was investigated. Benefiting from the Ru doping, $Na_{0.6}[Co_{0.78}Ru_{0.22}]O_2$

delivered a high discharge capacity of 163 mAh g^{-1} at 0.1 C, which is superior to that of $Na_{0.67}CoO_2$. Furthermore, using a combination of operando-XRD, X-ray absorption spectroscopy, and theoretical studies, it was demonstrated that the presence of Ru suppresses the formation of Na^+/ordering in the structure and also activates itself via a Ru^{4+}/Ru^{5+} and additional $O^{2-}/(O_2^{n-})$ redox process in the layered structural framework. As a result, higher capacity is delivered in $Na_{0.6}[Co_{0.78}Ru_{0.22}]O_2$ owing to the use of both cationic and anionic redox reactions. Our findings indicate the feasibility of designing new high-capacity cathode materials for sodium-ion batteries by using 4*d* elements.

4. Experimental Section

Synthesis: P2-type $Na_{0.67}CoO_2$ (NCO) and $Na_{0.6}[Co_{0.78}Ru_{0.22}]O_2$ (NCRO) powders were synthesized by the self-combustion method. Stoichiometric amounts of $Co(NO_3)_2{\cdot}6H_2O$ (98%, Sigma–Aldrich) and $NaNO_3$ (99.5%, Alfa) were mixed with citric acid (99.5%, Sigma-Aldrich) and sucrose (99.5%, Sigma–Aldrich) in a weight ratio of 1:0.2:0.05 (salts:citric acid:sucrose) in water. The mixture was then stirred for 1 h and heated at 120 °C to evaporate the solvent. Further dried powders were heated at 220 °C to induce self-combustion. The collected powders were preheated at 400 °C for 4 h in air to remove the residual organics, and the obtained powders were mixed with RuO_2 (ACROS Organics) in an agate mortar. Both the NCO and NCRO powders were calcined at 900 °C for 12 h in an air gas and then slowly cooled to room temperature.

Characterization: For characterization of the synthesized powders X-ray diffraction was conducted using X'Pert, PANalytical diffractometer with Cu Kα radiation in the scan range from 10° to 80°. Rietveld refinement was performed to analyze the obtained powder XRD patterns using the full proof program.[32] The particle morphologies of the synthesized materials were investigated using field-emission scanning electron microscopy (SEM; SU-8010, Hitachi) and high-resolution transmission electron microscopy (TEM; Jeol, JEM-ARM200F) combined with energy-dispersive X-ray spectroscopy (EDX). Operando XRD measurements (*o*-XRD, X'Pert, PANalytical diffractometer) were conducted to monitor the structural evolution during Na^+ de-/intercalation.[33,34] The direct-current electrical conductivity of both NCO and NCRO powders was measured by using the direct volt–ampere method (CMT-SR1000, AIT). Disc samples were contacted with a four-point probe during the measurement process. The atomic ratios of elements in the samples were examined by inductively coupled plasma-atomic emission spectroscopy (ICP-AES; OPTIMA 8300; Perkin-Elmer, USA). X-ray absorption near-edge structure (XANES) spectroscopy measurements were performed at the 8 C beamline for the Co K-edge, the 10 C beamline for the Ru K-edge, and the 4 C beamline for the O K-edge at the Pohang Accelerator Laboratory, South Korea. The Athena software package was used to process the XANES data, as described in the reference.[35]

Electrochemical Testing: Electrodes were prepared by mixing the active materials (80 wt.%), polyvinylidene fluoride (PVDF, 10 wt.%), and conducting agent (Super P, 10 wt.%) in *N*-methyl-2-pyrrolidone (NMP) solution. The well-mixed slurry was applied on Al foil using a doctor blade and then dried at 110 °C for 24 h. Discs were cut out of the dried electrodes (loading mass: ≈3 mg cm^{-2}). All the procedures for the electrode fabrication and handling were performed in a dry room. Half cells were fabricated in an Ar-filled glovebox, using Na metal as the counter electrode, in an R2032 coin-type cell. The electrolyte solution used was 0.5 M $NaPF_6$ in a mixture of propylene carbonate (PC) and fluorinated ethylene carbonate (FEC), with a volume ratio of 98:2. The electrochemical performance of each half cell was evaluated by applying a constant current of 23.5 mA g^{-1} (0.1 C) in the voltage range of 1.5–4.3 V at room temperature. Galvanostatic intermittent titration technique (GITT) measurements were performed by applying the repeated current pulses for 30 min at a rate of 0.05 C (11.75 mA g^{-1}) for charge/discharge followed by an open-circuit periods of 1 h in the voltage range of 1.5–4.3 V. Differential electrochemical mass spectrometry (DEMS) was conducted in a R2032 coin-type. The cell was charged and discharged at a current rate of 23.5 mA g^{-1} (0.1 C). Ar served as the carrier gas for charge and discharge processes at a flow rate of 15 sccm. Gas emissions were measured using HPR-20 R&D *O*-DEMS (Hiden Analytical).

First-Principles Calculations: Spin-polarized density functional theory (DFT) calculations with the projector augmented wave (PAW)[36] potential as implemented in the Vienna Ab Initio Simulation Package (VASP)[37] were performed for the undoped and doped Na_xCoO_2 materials for both fully charged and discharged states. The geometries of the structures were optimized using the Perdew–Burke–Ernzerhof (PBE)[38] functional and an electronic convergence criterion of 10^{-4} eV as well as a force convergence criterion of 2×10^{-2} eV $Å^{-1}$. PAW potentials containing only the valence electrons of the considered elements were used, and the energy cut off was set to 520 eV. The electronic structures were determined by single-point calculations with the Heyd–Scuseria–Ernzerhof (HSE) 06[39] functional. As the first step, four electronic optimizations with different initial magnetic moments (number of unpaired electrons) considering different redox activities of the metal ions as well as high- or low-spin configurations for cobalt ions were performed for each compound (Table S3, Supporting Information). An electronic convergence criterion of 10^{-2} eV was used, and the structures with the lowest energies were further converged to 10^{-4} eV for the final analysis. The Na and Ru contents as well as the structure types were adjusted to the experimental findings, resulting in the following models: $Na_{0.75}CoO_2$ (P2), $Na_{0.25}CoO_2$ (P2), $Na_{0.69}Ru_{0.25}Co_{0.75}O_2$ (P2), and $Na_{0.06}Ru_{0.25}Co_{0.75}O_2$ (OP4). Supercells of $4 \times 2 \times 1$ (*k*-point mesh: $2 \times 4 \times 2$) were used for the P2 phases, and a $2 \times 2 \times 1$ (*k*-point mesh: $4 \times 4 \times 1$) supercell was used for the OP4 phase, containing 16 formula units each. For the electronic-structure calculations, $Na_{0.06}Ru_{0.25}Co_{0.75}O_2$ was also modeled in the P2 phase, assuming that the inter-layer interactions could be neglected for the electronic structures. An HSE optimization with 10^{-3} eV electronic and 4×10^{-2} eV $Å^{-1}$ force convergence criteria as well as a reduced *k*-point grid of $1 \times 2 \times 1$ was performed for the P2 structure. The electronic structures of desodiated NCRO were obtained using this P2 model. The arrangements of the Na, Ru, and Co ions were determined using a coulomb-energy analysis with the help of the so-called supercell code.[40] The following charges were applied for the analysis: −2 for oxygen, +1 for sodium, +3 for cobalt, and +4 for ruthenium. The required additional positive charges for the charge balance were assigned evenly to cobalt and ruthenium ions. All possible Na arrangements were iterated together with the Ru and Co arrangements, and all possible distributions of Na ions between the two different P sites were considered, resulting in a full screening of all possible configurations, in total $\approx 10^{12}$ structures including symmetry equivalents. Atomistic structures were visualized with the VESTA software package,[41] and spin-density differences were calculated using the Vaspkit software.[42]

Supporting Information

Supporting Information is available from the Wiley Online Library or from the author.

Acknowledgements

This work was supported by the Basic Science Research Program through the National Research Foundation of Korea (NRF), funded by the Ministry of Education, Science, and Technology of Korea (NRF-2020R1A6A1A03043435, NRF-2023R1A2C2003210, and NRF-2022R1F1A1063351). This research was also supported by the Technology Innovation Program (Alchemist Project, 20012196, AI-based supercritical materials discovery) and HRD Program for Industrial Innovation (P0023521) funded by the Ministry of Trade, Industry and Energy, Korea. P.K. acknowledges the financial support of the German Research Foundation (DFG) with project number 501562980 as well as the computing time granted through JARA-HPC on the supercomputer JURECA at Forschungszentrum Jülich.

Conflict of Interest

The authors declare no conflict of interest.

Data Availability Statement

The data that support the findings of this study are available from the corresponding author upon reasonable request.

Keywords

anionic, batteries, cathodes, cationic, redox, sodium

Received: June 26, 2023
Revised: July 27, 2023
Published online: August 17, 2023

[1] C. Fouassier, G. Matejka, J. M. Reau, P. Hagenmuller, *J. Solid State Chem.* **1973**, *6*, 532.
[2] T. Motohashi, E. Naujalis, R. Ueda, K. Isawa, M. Karppinen, H. Yamauchi, *Appl. Phys. Lett.* **2001**, *79*, 1480.
[3] C. Delmas, J.-J. Braconnier, C. Fouassier, P. Hagenmuller, *Solid State Ionics* **1981**, *3/4*, 165.
[4] K. Mizushima, P. C. Jones, P. J. Wiseman, J. B. Goodenough, *Mater.Res.Bull* **1980**, *15*, 783.
[5] Y. Lei, X. Li, L. Liu, G. Ceder, *Chem. Mater.* **2014**, *26*, 5288.
[6] T. Shibata, Y. Fukuzumi, W. Kobayashi, Y. Moritomo, *Sci. Rep.* **2015**, *5*, 8.
[7] R. Berthelot, D. Carlier, C. Delmas, *Nat. Mater.* **2011**, *10*, 74.
[8] M. Bianchini, J. Wang, R. Clément, G. Ceder, *Adv. Energy Mater.* **2018**, *8*, 1801446.
[9] D. Carlier, J. H. Cheng, R. Berthelot, M. Guignard, M. Yoncheva, R. Stoyanova, B. J. Hwang, C. Delmas, *Dalton Trans.* **2011**, *40*, 9306.
[10] J.-H. Cheng, C.-J. Pan, J.-F. Lee, J.-M. Chen, M. Guignard, C. Delmas, D. Carlier, B.-J. Hwang, *Chem. Mater.* **2014**, *26*, 1219.
[11] X. Wang, M. Tamaru, M. Okubo, A. Yamada, *J. Phys. Chem. C* **2013**, *117*, 15545.
[12] N. Voronina, H. J. Kim, M. Shin, S. Myung, *J. Power Sources* **2021**, *514*, 230581.
[13] S. M. Kang, J. H. Park, A. Jin, Y. H. Jung, J. Mun, Y. E. Sung, *ACS Appl. Mater. Interfaces* **2018**, *10*, 3562.
[14] N. Sabi, A. Sarapulova, S. Indris, H. Ehrenberg, J. Alami, I. Saadoune, *ACS Appl. Mater. Interfaces* **2017**, *9*, 37778.
[15] S. C. Han, H. Lim, J. Jeong, D. Ahn, W. B. Park, K. S. Sohn, M. Pyo, *J. Power Sources* **2015**, *277*, 9.
[16] M. Matsui, F. Mizukoshi, N. Imanishi, *J. Power Sources* **2015**, *280*, 205.
[17] X. Cao, H. Li, Y. Qiao, X. Li, M. Jia, J. Cabana, H. Zhou, *Adv. Energy Mater.* **2020**, *10*, 1903785.
[18] N. Voronina, N. Yaqoob, H. J. Kim, K. S. Lee, H. D. Lim, H. G. Jung, O. Guillon, P. Kaghazchi, S. T. Myung, *Adv. Energy Mater.* **2021**, *11*, 2100901.
[19] M. Jia, Y. Qiao, X. Li, K. Jiang, H. Zhou, *J. Mater. Chem. A* **2019**, *7*, 20405.
[20] M. Tamaru, X. Wang, M. Okubo, A. Yamada, *Electrochem. Commun.* **2013**, *33*, 23.
[21] B. Mortemard de Boisse, M. Reynaud, J. Ma, J. Kikkawa, S. ichi Nishimura, M. Casas-Cabanas, C. Delmas, M. Okubo, A. Yamada, *Nat. Commun.* **2019**, *10*, 2185
[22] N. Voronina, M. Shin, H. Kim, N. Yaqoob, O. Guillon, S. H. Song, H. Kim, H. Lim, H. Jung, Y. Kim, H. Lee, K. Lee, K. Yazawa, K. Gotoh, P. Kaghazchi, S. Myung, *Adv. Energy Mater.* **2022**, *2103939*, 2103939.
[23] S. Song, M. Kotobuki, F. Zheng, Q. Li, C. Xu, Y. Wang, W. D. Z. Li, N. Hu, L. Lu, *J. Power Sources* **2017**, *342*, 685.
[24] J. Martinez De Ilarduya, L. Otaegui, J. M. López del Amo, M. Armand, G. Singh, *J. Power Sources* **2017**, *337*, 197.
[25] B. Zhang, R. Dugas, G. Rousse, P. Rozier, A. M. Abakumov, J. M. Tarascon, *Nat. Commun.* **2016**, *7*, 10308.
[26] M. Sathiya, J. Thomas, D. Batuk, V. Pimenta, R. Gopalan, J. M. Tarascon, *Chem. Mater.* **2017**, *29*, 5948.
[27] J. H. Jo, J. U. Choi, Y. J. Park, J. K. Ko, H. Yashiro, S. T. Myung, *Energy Storage Mater.* **2020**, *32*, 281.
[28] G. Singh, N. Tapia-Ruiz, J. M. Lopez Del Amo, U. Maitra, J. W. Somerville, A. R. Armstrong, J. Martinez De Ilarduya, T. Rojo, P. G. Bruce, *Chem. Mater.* **2016**, *28*, 5087.
[29] J. Y. Hwang, J. Kim, T. Y. Yu, Y. K. Sun, *Adv. Energy Mater.* **2019**, *9*, 1803346.
[30] Z. Cheng, B. Zhao, Y. J. Guo, L. Yu, B. Yuan, W. Hua, Y. X. Yin, S. Xu, B. Xiao, X. Han, P. F. Wang, Y. G. Guo, *Adv. Energy Mater.* **2022**, *12*, 2103461.
[31] J. Zheng, S. Myeong, W. Cho, P. Yan, J. Xiao, C. Wang, J. Cho, J. G. Zhang, *Adv. Energy Mater.* **2017**, *7*, 1601284.
[32] J. Rodríguez-Carvajal, *Phys. B* **1993**, *192*, 55.
[33] N. Voronina, J. H. Jo, J. U. Choi, A. Konarov, J. Kim, S. T. Myung, *J. Power Sources* **2020**, *455*, 227976.
[34] H. J. Kim, J. H. Jo, J. U. Choi, N. Voronina, S. T. Myung, *J. Power Sources* **2020**, *478*, 229072.
[35] B. Ravel, M. Newville, *J. Synchrotron Radiat.* **2005**, *12*, 537.
[36] P. E. Blöchl, *Phys. Rev. B* **1994**, *50*, 17953.
[37] G. Kresse, J. Furthmüller, *Phys. Rev. B* **1996**, *54*, 11169.
[38] J. P. Perdew, K. Burke, M. Ernzerhof, *Phys. Rev. Lett.* **1996**, *77*, 3865.
[39] A. V. Krukau, O. A. Vydrov, A. F. Izmaylov, G. E. Scuseria, *J. Chem. Phys.* **2006**, *125*, 224106.
[40] K. Okhotnikov, T. Charpentier, S. Cadars, *J. Cheminf.* **2016**, *8*, 17.
[41] K. Momma, F. Izumi, *J. Appl. Crystallogr.* **2008**, *41*, 653.
[42] V. Wang, N. Xu, J.-C. Liu, G. Tang, W.-T. Geng, *Comput. Phys. Commun.* **2021**, *267*, 108033.